

Discrete dislocation dynamics by an $O(N)$ algorithm

Anders Jonsson *

Department of Solid Mechanics, Royal Institute of Technology, SE-100 44 Stockholm, Sweden

Received 17 November 2001; received in revised form 14 May 2002; accepted 7 September 2002

Abstract

An efficient numerical algorithm for discrete dislocation dynamics simulations in two-dimensional, finite polygonal domains is presented. The algorithm is based on a complex boundary integral equation method. By use of the fast multipole method, linear complexity and storage requirement are achieved. This method has not, to the present author's knowledge, previously been used in such simulations. Convergence studies show that the algorithm is accurate and numerically stable. Results from uniaxial load and bending moment load simulations at different loading rates are presented. The effect of finite size is studied. The results show that higher loading rate gives less yielding, and that a smaller specimen is harder than a larger one. This is in agreement with well-known results, and demonstrates that the dislocation dynamics model can describe important features of the physical problem. The cut-off velocity, that is the maximum velocity of the dislocations, is an important model parameter. In the present paper, it is shown that a four times higher cut-off velocity than was previously deemed sufficient is needed to obtain results independent of the cut-off velocity for the bending moment load simulations.

© 2002 Elsevier Science B.V. All rights reserved.

Keywords: Dislocations; Plasticity; Size effect; Fast multipole method; Numerical simulations; Efficient algorithm

1. Introduction

Plastic deformation is caused by movement of a large number of defects in the crystal lattice, so-called dislocations. If a sufficiently small specimen is studied, the motion of individual dislocations will be of importance to the plastic deformation. Due to this, there will be a size effect on the plastic behavior of a material. This has been observed in experiments, see for example Refs. [1,2].

Conventional continuum plasticity theory is successful in describing the global plastic behavior of materials at the macro-scale. In the meso-length scale, that is in the range 0.1–100 μm , finite size effects become pronounced. The meso-scale is of interest for example in micro-electro-mechanical and micro-electronics applications. The conventional theory lacks a material length scale, and predicts the same response independent of the size of the studied specimen. It is unable to describe the material response at small ($\leq 100 \mu\text{m}$) length scales. Much attention has therefore been paid on the development of so-called non-local plasticity theories, see for example Refs. [3–8] for a review.

* Tel.: +46-8-7908397; fax: +46-8-4112418.

E-mail address: andersj@half.kth.se (A. Jonsson).

These theories involve one or more length scales in different ways.

Further development of plasticity theories requires a firm understanding of the mechanisms behind plastic deformation at small length scales. This is also of fundamental interest in materials science. Discrete dislocation dynamics simulations can serve as a tool to increase this understanding. In such simulations, the plastic deformation is modeled by the movement of individual dislocations in the material, and length scales are introduced in a natural way.

The numerical simulation of dislocation dynamics has been associated with lengthy computations [9]. When computing the interaction forces between N dislocations using a direct method, the computation cost will be $O(N^2)$. Since a large number of dislocations ($N \sim 10^3$) is easily obtained in a simulation, using a direct method will be time and storage consuming. Also, a very large number of increments is needed for each complete simulation, and it is necessary to solve each increment as fast as possible in order to avoid unreasonable execution times. A number of parameter values must be chosen in a discrete dislocation model, see for example Refs. [10–13]. In order to be able to determine the effects of these parameters on the simulation results, controllable accuracy is needed. In order to make the simulations more realistic, there is a need to add an increasing number of features to the model. This makes the computations more involved, and will increase the need for fast methods. To make large scale dislocation dynamics simulations using increasingly complicated models possible, linear complexity, speed and accuracy in the numerical algorithm are necessary.

This paper presents a step on the way. A numerical algorithm is presented, where the computation cost and storage requirement is $O(N_{\text{tot}})$, where N_{tot} is the sum of the number of dislocations, dislocation sources and discretization points. This is achieved by use of the fast multipole method (FMM), see Refs. [14,15]. Controllable accuracy is obtained by use of a stable numerical method. The present algorithm is used for studying loading rate and size effects on uniaxial tensile loading and bending moment loading of a finite

specimen. The FMM has not, to the present author's knowledge, previously been used in a discrete dislocation simulation of a finite specimen. An $O(N)$ algorithm for dislocation dynamics in 2D with periodic boundary conditions has previously been presented by Wang and LeSar, see Ref. [16]. The cut-off velocity, that is the maximum velocity of the dislocations, is an important model parameter. In the present paper, the cut-off velocity is increased a factor eight compared to previous simulations, see Ref. [11], in a parameter study. For the bending moment loading simulations, a four times higher cut-off velocity than was previously deemed sufficient is needed to obtain results independent of the cut-off velocity.

This paper is organized as follows. In Section 2, the boundary value problem for a linear elastic, two-dimensional and finite solid is formulated. The solution of the boundary value problem using complex valued potential theory is also outlined. The dislocation dynamics procedure is explained in Section 3. In Section 4, the numerical solution scheme is presented. Numerical results from uniaxial load and bending moment load simulations of a finite specimen at different loading rates are given in Section 5. Graphs of stress–strain and moment–rotation curves, dislocation positions and densities are presented for different loading rates. The effect of the specimen size is also studied. Controlled accuracy is used. The influence of some of the model parameters is investigated. Finally, some conclusions are made in Section 6.

2. Boundary value problem

A single crystal will be considered. Grain boundary effects are not included. Effects of temperature or hydrogen content on the dislocation mobility will also not be considered.

A linear elastic, isotropic material model is used. The material occupies a two-dimensional domain D with boundary Γ . Small strain is assumed. The shear modulus is μ and the plane strain bulk modulus is κ . The Poisson's ratio is ν . A plane strain analysis of the single crystal containing edge dislocations is performed. Traction t^{pr} is prescribed at the boundary, see Fig. 1.

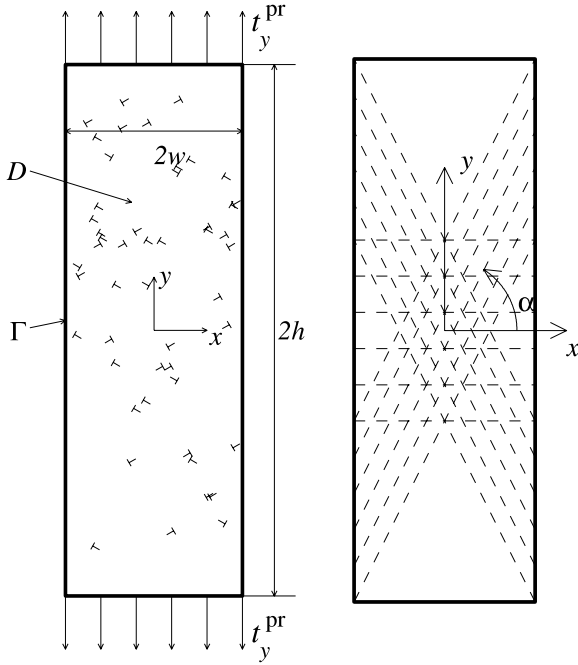


Fig. 1. Left: An elastic rectangle, width $2w$ and height $2h$ containing N edge dislocations, marked with 'T's. Traction t_y^{pr} is prescribed on the short sides, while the long sides are traction free. Right: Placement of slip systems, indicated by the dashed lines.

2.1. Formulation

Initially, the domain is free from dislocations. During the course of loading, dislocations are created, removed and allowed to move, see Section 3. The number of currently present dislocations is N . The boundary value problem is solved in an incremental fashion using a cumulative superposition technique, see Refs. [10–13]. For each increment, the traction t^d at the boundary Γ from the dislocations is calculated. This traction with opposite sign, together with the currently prescribed traction t^{pr} is applied, and the boundary value problem with these modified boundary conditions is solved. Stress, strain, and displacement fields are obtained by superposition of the fields from the dislocations and the fields from the elastic solution to the boundary value problem. The fields from the dislocations correspond to those in infinite space. This can be formulated as a modified boundary value

$$t = t^{pr} - t^d \quad (1)$$

for the prescribed traction vector. The increments in strain, stress and displacement are superposed according to

$$\begin{aligned} \Delta\sigma &= \Delta\sigma^e + \Delta\sigma^d, & \Delta\epsilon &= \Delta\epsilon^e + \Delta\epsilon^d, \\ \Delta u &= \Delta u^e + \Delta u^d. \end{aligned} \quad (2)$$

In Eqs. (1) and (2), superscript d denotes contributions from the dislocations, and superscript e denotes contributions from the elastic solution.

2.2. Complex-valued potential method

The boundary value problem of Eq. (1) is solved using a complex-valued potential method. For a thorough discussion of the complex variable approach to elasticity problems, see Refs. [17–20]. For a textbook on dislocations and their properties, see for example Ref. [21].

In the following, $z = x + iy$ will denote the complex variable. The potentials $\Phi(z)$ and $\Psi(z)$ are introduced, related to the components of the stress field σ^e as

$$\sigma_{xx}^e + \sigma_{yy}^e = 4\Re\{\Phi(z)\}, \quad (3)$$

$$\sigma_{yy}^e - \sigma_{xx}^e + 2i\sigma_{xy}^e = 2(\bar{z}\Phi'(z) + \Psi(z)), \quad (4)$$

where overbar represents conjugation. The boundary value problem will be solved using a Fredholm second-kind integral equation, see Ref. [22] for a thorough discussion and Ref. [23] for an application. From the Cauchy-type integral representations

$$\Phi(z) = \frac{1}{2\pi i} \int_{\Gamma} \frac{\Phi(\tau) d\tau}{(\tau - z)}, \quad z \in D, \quad (5)$$

and

$$\begin{aligned} \psi(z) &= -\frac{1}{2\pi i} \int_{\Gamma} \frac{\overline{\Phi(\tau)} d\bar{\tau}}{(\tau - z)} - \frac{1}{2\pi i} \int_{\Gamma} \frac{\bar{\tau}\Phi(\tau) d\tau}{(\tau - z)^2} \\ &\quad - \frac{1}{2\pi i} \int_{\Gamma} \frac{\bar{m} d\tau}{(\tau - z)}, \quad z \in D, \end{aligned} \quad (6)$$

the following Fredholm second-kind integral equation can be derived,

$$(I - M_3 + iQ_1)\Phi(z) = Hnt(z), \quad z \in \Gamma, \quad (7)$$

where $n = n_x + in_y$ is the outward normal of D . In Eq. (7), M_3 is a compact integral operator given by

$$M_3 f(z) = \frac{1}{2\pi i} \left[\int_{\Gamma} \frac{f(\tau) d\tau}{(\tau - z)} + \frac{\bar{n}}{n} \int_{\Gamma} \frac{f(\tau) d\tau}{(\bar{\tau} - \bar{z})} + \int_{\Gamma} \frac{\overline{f(\tau)} d\bar{\tau}}{(\bar{\tau} - \bar{z})} + \frac{\bar{n}}{n} \int_{\Gamma} \frac{(\tau - z) \overline{f(\tau)} d\bar{\tau}}{(\bar{\tau} - \bar{z})^2} \right], \quad z \in \Gamma. \quad (8)$$

The operator H in Eq. (7) acting on a function f is given by

$$Hf(z) = \frac{\bar{n}}{2n} f(z) + \frac{\bar{n}}{2n} \frac{1}{\pi i} \int_{\Gamma} \frac{f(\tau) d\bar{\tau}}{(\bar{\tau} - \bar{z})}, \quad z \in \Gamma. \quad (9)$$

The operator Q_1 in Eq. (7) is a mapping from Γ to \mathbb{R} , defined as

$$Q_1 f = -\frac{1}{2A} \Re e \left\{ \int_{\Gamma} f(\tau) \bar{\tau} d\tau \right\}, \quad (10)$$

where A is the area of the domain D .

The stress field from the dislocations, σ^d , can be expressed in a similar way as in Eqs. (3) and (4),

$$\sigma_{xx}^d + \sigma_{yy}^d = 4\Re e\{S_1(z)\}, \quad (11)$$

$$\sigma_{yy}^d - \sigma_{xx}^d - 2i\sigma_{xy}^d = 2S_2(z), \quad (12)$$

where

$$S_1(z) = \frac{1}{2i} \sum_{j=1}^N \frac{d_j}{(z - t_j)}, \quad (13)$$

$$S_2(z) = \frac{1}{2i} \sum_{j=1}^N \left(\frac{d_j}{(\bar{z} - \bar{t}_j)} + \frac{\bar{d}_j(z - t_j)}{(\bar{z} - \bar{t}_j)^2} \right) \quad (14)$$

and t_k is the position of dislocation k . The stress field obtained through Eqs. (11)–(14) corresponds to the stress field of dislocation in infinite space. Complex-variable notation is used in analogy with Eqs. (3) and (4), see further Remark 2.1 below. If $z = t_k$ in Eqs. (13) and (14), the term $j = k$ is omitted. The k th dislocation is characterized by the quantity

$$d_k = \frac{\mu\kappa}{\pi(\mu + \kappa)} b_k e^{i\alpha_k}, \quad (15)$$

where b_k is the strength of the dislocation, and α_k is the angle of the slip plane. The quantity $\mathbf{b}_k = b_k e^{i\alpha_k}$ is the Burgers vector of the k th dislocation.

With the notation of Eqs. (11)–(14), the total prescribed traction of Eq. (1) can be expressed as

$$nt(z) = nt^{\text{pr}}(z) - n^2 \Re e\{S_1(z)\} + S_2(z), \quad z \in \Gamma. \quad (16)$$

The displacement at the boundary can be obtained as

$$u_x(z) + iu_y(z) = \frac{\mu + \kappa}{\mu\kappa} \int_{z_0}^z [\Phi(\tau) + S_1(\tau)] d\tau - \frac{1}{2\mu} \int_{z_0}^z \bar{n} t^{\text{pr}}(\tau) d\tau + \hat{\delta}(z), \quad z \in \Gamma. \quad (17)$$

If dislocations are present, the function $\hat{\delta}(z)$ of Eq. (17) assures that the discontinuities in the displacement from each dislocation is properly aligned with the slip plane direction.

Remark 2.1. It can be noted that the integral representations of Eqs. (5) and (6) are quite similar to the sums S_1 and S_2 of Eqs. (13) and (14). It is possible to express the discretized version of M_3 by sums with identical appearance as S_1 and S_2 . This makes it possible to use the FMM already developed for the operator M_3 , for computing S_1 and S_2 , with only slight modifications.

3. Dislocation dynamics

Dislocation dynamics simulations in 2D was pioneered by, amongst others, Gulluoglu et al. [24], Lepinoux and Kubin [25], and Gulluoglu and Hartley [26,27]. Recent work has been done by, amongst others, Needleman and co-workers, see Refs. [10–13,28]. For an overview, see Ref. [9]. In this section, the rules controlling dislocation creation, movement and removal are presented. Basically, the same strategy as used in Refs. [10–13] is employed.

The Peach–Koehler force (dislocation sliding force per unit length) $f_k = f(t_k)$ on dislocation k can be evaluated as

$$f_k = \frac{b_k}{2} [(\sigma_{xx} - \sigma_{yy}) \sin 2\alpha_k - 2\sigma_{xy} \cos 2\alpha_k]. \quad (18)$$

In the present setting, using Eqs. (3), (4), (11) and (12) the expression of Eq. (18) can be put as

$$f_k = b_k \Im \{ S_2(t_k) e^{-2i\alpha_k} - (\bar{t}_k \Phi'(t_k) + \Psi(t_k)) e^{2i\alpha_k} \}. \quad (19)$$

A total of N_s dislocation sources are placed randomly on the slip planes of the three slip systems, see the right image of Fig. 1. The source density ρ_s is defined as $\rho_s = N_s/A$. First, one of the three slip systems is chosen randomly. Then, a slip plane within that slip system is chosen randomly. Finally, the source is placed randomly on that slip plane. Uniform random distributions are used in the placement of the sources. The location of the dislocation sources are denoted as s_k . The slip plane spacing is chosen as $d_{sp} = 100b$ within each slip system. The physical slip plane spacing in a crystal might be less than this, but since the spacing between active slip planes is much coarser than $100b$, see Ref. [11] and Section 5.2, this choice implies no restriction. The three slip systems makes angles $\alpha = 0, \pi/3, 2\pi/3$ with the x -axis, see Fig. 1. The sources produce a dislocation pair at time T_0 , if the sliding force exceeds a critical nucleation strength f_k^{nuc} during the time T_{nuc} , that is

$$|f(s_k, T)| \geq f_k^{\text{nuc}} \quad \forall T \in [T_0 - T_{\text{nuc}}, T_0].$$

The nucleation strengths are also chosen randomly from a normal distribution with mean value f_{mean} and standard deviation f_{std} . The created dislocation pair consists of two dislocations with opposite Burgers vector, located symmetrically with respect to s_k at a distance

$$L_k^{\text{nuc}} = \frac{\mu}{2\pi(1-\nu)} \frac{b^2}{f_k^{\text{nuc}}} \quad (20)$$

from each other. At this distance the interaction forces from one dislocation on the other is exactly balanced by the slip plane shear stress.

Two dislocations, say m and n , $n > m$, are removed if they come within a specified distance L_e to each other, $|t_m - t_n| < L_e$. If the sum of the Burgers vectors $\mathbf{b}_k = \mathbf{b}_m + \mathbf{b}_n \neq \mathbf{0}$, a new dislocation with Burgers vector \mathbf{b}_k is created, located at t_n . A more natural location of the new dislocation

would be $t_k = (t_m + t_n)/2$, but since $|t_k - t_n| < L_e/2 = 3b$, it is estimated that the difference is without effect to the simulation results. A single dislocation that is closer than $3L_e/2$ to the domain boundary is also removed. This distance is motivated by numerical reasons; it is chosen to avoid that dislocations coincide with the boundary. Steps left at the surface created by exiting dislocations are accounted for in an appropriate way.

The dislocation velocities are calculated by a drag relation and a cut-off velocity v_{max} ,

$$v_k = \min\{C_v^{-1}|f_k|, v_{\text{max}}\} \text{sign } f_k, \quad (21)$$

where C_v is the drag coefficient. The dislocation dynamics simulation is carried out in an incremental fashion. The time is discretized, $T^j = j\Delta T$. The time step ΔT is kept constant throughout the whole simulation. In one time step, that is from T^j to T^{j+1} , the dislocations are moved according to

$$t_k^{j+1} = t_k^j + e^{i\alpha_k} v_k \Delta T, \quad (22)$$

which in some sense can be seen as an Euler-forward scheme. The dislocations are only allowed to move in the slip plane directions, and no movement normal to the slip planes (climb) is allowed in the present model. In future work, dislocation climb will also be included, in order to study effects of this.

The applied load is increased in each time step,

$$t^{\text{pr},j+1} = t^{\text{pr},j} + \dot{t}^{\text{pr}} \Delta T, \quad (23)$$

where \dot{t}^{pr} is the prescribed loading rate.

Remark 3.1. By implementing the dislocation dynamics according to the above, three non-dimensional lengths are introduced in the model: the slip plane spacing to Burger's vector ratio d_{sp}/b (100 in the present case), the ratio between Burger's vector and the size (e.g. length or width) of the specimen and the mean distance between dislocation sources to d_{sp} ratio. Another non-dimensional length arises from the numerical solution procedure, namely $v_{\text{max}}\Delta T/L_e$, that is the ratio between the maximum distance one dislocation is allowed to move in one time step and the removal distance.

Remark 3.2. The Euler forward scheme with a constant ΔT of Eq. (22) is preferred here for its simplicity. It is only first order accurate, and

higher order time integration schemes, for example of Runge–Kutta type, will be considered in forthcoming work.

4. Method of solution

The method of solution can be summarized as follows:

- A simple time-stepping scheme as described in Section 3 is used to simulate the behavior of individual dislocations.
- A Nyström scheme is used for solving the integral equation of Eq. (7) in each time step.
- Combination of the FMM and an iterative solver (GMRES) results in linear complexity.
- A priori mesh refinement is used to increase the accuracy.

A more detailed description is given below and in the References.

4.1. A priori mesh refinement

Initially, the boundary is divided into j panels Γ_k of approximately equal length, see Fig. 2,

$$\Gamma = \bigcup_{k=1}^j \Gamma_k, \quad |\Gamma_k| \approx \frac{1}{j} |\Gamma|.$$

To improve convergence, panels next to corner panels are divided into two. In order to reduce the discretization error, an ad hoc a priori mesh refinement method based on Legendre expansions is used. The coefficients c_k in the local Legendre expansion of the discretized right-hand side of Eq. (7) is computed,

$$\text{Hnt}(z) \approx \sum_{l=1}^8 c_l P_l(s), \quad z \in \Gamma_k, \quad s \in [-1, 1], \quad (24)$$

where s is a local coordinate on Γ_k , and P_l is the l th order Legendre polynomial. The ratio $r = (|c_7| + |c_8|)/(|c_1| + |c_2|)$ is used as a measure of how well the right-hand side is resolved. If $r > \epsilon_{\text{ref}}$ on a panel, the panel is divided into two panels of equal length. This is done for all panels. Then the right-hand side on the new mesh is computed, and

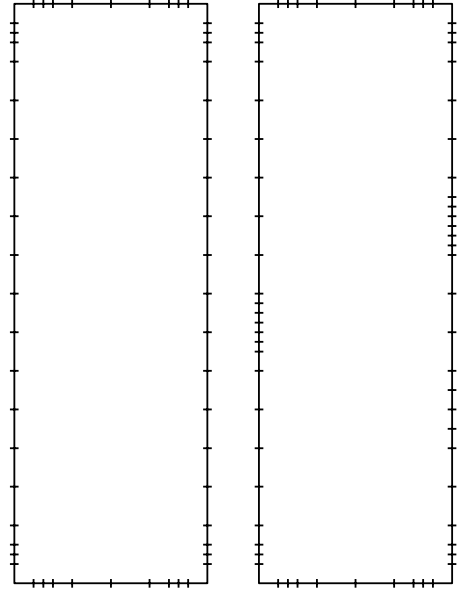


Fig. 2. The boundary is divided into panels. Left: Uniform discretization (schematic). Right: A priori mesh refinement (schematic) is used in order to reduce the discretization error. Panels where the right-hand side is varying rapidly are divided in two.

the refinement procedure is repeated. In practice, this means that panels where the right-hand side is varying rapidly, typically when a dislocation comes close to the boundary, will be divided. This procedure will tend to minimize the constant C in the error estimate of Eq. (29). The a priori refinement is performed for each time step. A similar refinement strategy has been used in Refs. [29,30].

4.2. Nyström scheme

The integral equation of Eq. (7) is solved numerically. A Nyström discretization scheme with eight point composite Gauss–Legendre quadrature is used. For modern textbooks on the use of Nyström discretization for the solution of integral equations, see Chapter 4 of Ref. [31] or Section 4.7 of Ref. [32]. Eight discretization points z_k , are placed on each panel Γ_k . Totally $N_p = 8j$ discretization points are placed on the boundary. On the corner panels, the density $\Phi(z)$ is represented using special basis functions of the form

$$\Phi_n(z)_{\text{symm}} = f_n z^{\lambda_n-1} + \bar{f}_n z^{\bar{\lambda}_n-1} \quad (25)$$

and

$$\Phi_n(z)_{\text{anti-symm}} = g_n z^{\mu_n-1} - \bar{g}_n z^{\bar{\mu}_n-1}, \quad (26)$$

where f_n and g_n are complex coefficients and λ_n and μ_n are a mix of positive integer exponents and widely spaced non-integer exponents given by the Williams solution [33]. See Refs. [23,34] for more details on the implementation of the corner panels. See Figs. 3 and 4 for a schematic of how the discretization points are placed on corner panels and regular boundary panels.

Once the boundary is discretized, the next step in the Nyström discretization scheme is to approximate the integrals of Eq. (7) (the operators H and M_3) over Γ by sums over the N_p discretization points. This yields, very schematically,

$$x_m - \sum_{k=1}^{N_p} M_{mk} x_k w_k = \sum_{k=1}^{N_p} H_{mk} n_k t_k w_k, \quad (27)$$

$$m = 1, 2, \dots, N_p$$

or, using matrix notation,

$$(\mathbf{I} - \mathbf{M})\mathbf{x} = \mathbf{H}\mathbf{q}, \quad (28)$$

where, in principle, x_k denotes the pointwise approximation of the unknown density $\Phi(z)$ and w_k corresponds to integration weights. The components of the vector \mathbf{q} are $q_k = n_k \cdot t_k$.

The order of accuracy in the discretization of the operators H and M_3 of Eq. (7) is estimated to be asymptotically 6.85. This is due to the presence of corners. On smooth boundaries, the operator M_3 is 16th order and H is 8th order. The error in

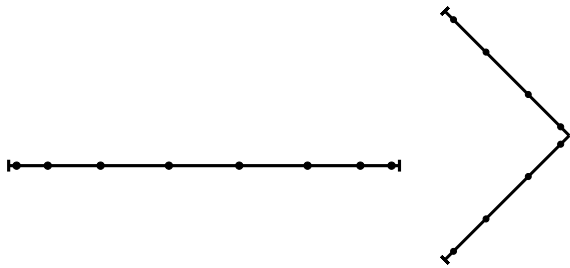


Fig. 3. Discretization points (●) are placed on the panels (—) according to a eight point composite Gauss–Legendre quadrature. Left: A regular boundary panel. Right: A corner panel.

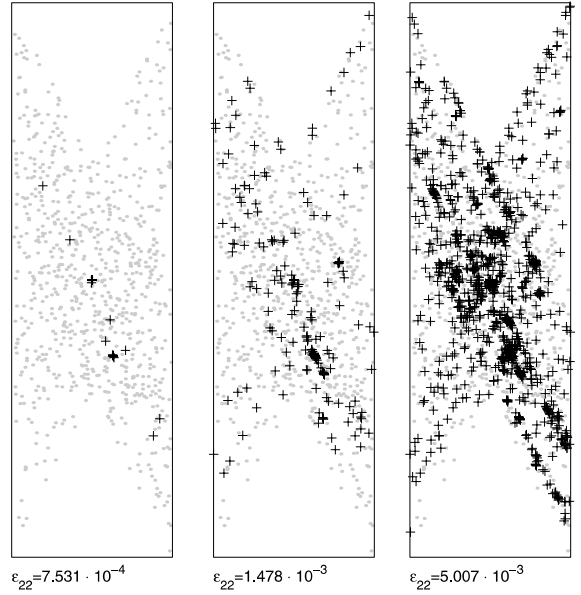


Fig. 4. Dislocation positions, indicated by '+', at different strain levels. Dislocation sources are shown as grey dots.

the approximate solution x_k can in the present case be estimated by

$$\|x_k - \Phi\| \leq C j^{-6.85}, \quad (29)$$

where C depends on the known right-hand side and the discretization. The a priori mesh refinement of Section 4.1 is intended to minimize this constant.

4.3. Iterative solver and the FMM

This section describes the solution of Eq. (28). Since the right-hand side of Eq. (28) changes between the time steps, the equation must also be solved for each time step.

A direct solver finds a complete factorization of the matrix $\mathbf{I} - \mathbf{M}$. Since $\mathbf{I} - \mathbf{M}$ is a full matrix, the computational cost for this is $O(N_p^3)$. A large number of time steps and discretization points are needed for accuracy, and a computational cost of $O(N_p^3)$ means unacceptably long execution times of the simulations.

The GMRES [35] iterative solver is used here for solving Eq. (28). In principle, GMRES finds an

incomplete factorization of the matrix $\mathbf{I} - \mathbf{M}$ and an approximative solution (within a specified tolerance) of Eq. (28). This is, roughly speaking, obtained by multiplying $\mathbf{I} - \mathbf{M}$ by a trial vector $\hat{\mathbf{x}}_k$ in each iteration,

$$(\mathbf{I} - \mathbf{M})\hat{\mathbf{x}}_1, (\mathbf{I} - \mathbf{M})\hat{\mathbf{x}}_2, \dots, (\mathbf{I} - \mathbf{M})\hat{\mathbf{x}}_{N_{\text{iter}}}. \quad (30)$$

In the present case, the main work of the GMRES solver is performing the N_{iter} matrix–vector products, where $N_{\text{iter}} \ll N_p$, which would mean a computational cost of $O(N_p^2)$. This still would mean very long execution times of the simulations.

Since the matrices \mathbf{M} and \mathbf{H} are obtained from discretizations of integral operators similar to layer potentials, the FMM [14,15] can be used with only minor modifications, see Ref. [30], for performing the matrix–vector products of Eq. (30) and the right-hand side of Eq. (28) in an approximative way, within a specified tolerance. This means that the computational cost will be directly proportional, $O(N_p)$, to the number of unknowns when solving Eq. (28). A computational cost of $O(N_p)$ is necessary in order to obtain acceptable simulation times. The solution from the previous time step is used as an initial trial vector, if the mesh has not been refined in the current time step, reducing the simulation time further by typically about 20%.

The sums S_1 , and S_2 of Eqs. (13) and (14) must be computed in the points t_k , $k = 1, \dots, N$ and s_k , $k = 1, \dots, N_s$ but also on the boundary points z_k , $k = 1, \dots, N_p$. This is also done by use of the FMM, resulting in a computational cost that is $O(N_{\text{tot}})$, where $N_{\text{tot}} = N + N_s + N_p$.

Computing the sliding force of Eq. (19) involves computing $\Phi'(z)$ and $\Psi(z)$ when $z \in D$, which means that the integrals of Eqs. (5) and (6) must be evaluated in the points t_k and s_k , that is totally $N_s + N$ times, from the values $\Phi(z_k)$, $k = 1, \dots, N_p$. These integrals are computed numerically using the FMM, resulting in a computational cost that is $O(N_{\text{tot}})$.

5. Numerical results

Results from uniaxial tension (Section 5.1) and bending (Section 5.2) simulations at different loading rates are presented. Effect of finite size is

also studied, see Section 5.3. The numerical parameter values chosen are identical to those in Ref. [11], making comparisons of the results easier. Elastic material parameters are Young's modulus $E = 70$ GPa and Poisson's ratio $\nu = 0.33$. These material parameters correspond to $\mu = 26.3$ GPa and $\kappa = 77.4$ GPa under plane strain conditions. The drag coefficient is taken as $C_v = 10^{-4}$ Pa s. The length of the Burgers vector for each dislocation is taken as $b = 0.25$ nm. The distance L_e , that controls dislocation removal, is taken as $6b$. For the dislocation sources, $f_{\text{mean}}/b = 50$ MPa and $f_{\text{std}}/b = 10$ MPa is used. The nucleation time is set to $T_{\text{nuc}} = 10$ ns. A source density $\rho_s = N_s/A = 101/6 \mu\text{m}^2$ is used.

The maximum distance one dislocation can move in one time step, $L_s = v_{\text{max}}\Delta T$, must not be too long, or else possible dislocation interactions might be missed. In Sections 5.1–5.3 the cut-off velocity $v_{\text{max}} = 20$ m/s is chosen, and a constant time step $\Delta T = 5 \times 10^{-10}$ is used. These choices of ΔT and v_{max} result in $L_s = 5L_e$. These values have been used previously, see Ref. [11], and were then considered sufficient in order not to affect simulation results. In Section 5.5, the effect of increased v_{max} and reduced ΔT and L_s is studied.

A tolerance of 10^{-7} is used for the GMRES iterative solver, and a tolerance of 10^{-8} for the FMM. Typically, about 22 GMRES iterations are enough to obtain a relative accuracy of 10^{-7} .

As can be seen from Fig. 5, the time for performing the different parts of one simulation time step is proportional to the number of components, N , N_s or N_p , involved in the computation. The complexity of the algorithm is $O(N_{\text{tot}})$, where $N_{\text{tot}} = N + N_p + N_s$. This is due to the use of the FMM in many stages of the algorithm.

The accuracy in term of the spatial discretization is chosen so that the resulting force–displacement curves are reasonably smooth, but still as low as possible in order to minimize execution time. This means a relative error in the computed strain for a given dislocation configuration at a prescribed stress on the order of 5×10^{-4} , and on the order of 5×10^{-5} in the computed rotation for a prescribed moment. See further Section 5.5 and Section 5.4 for more details on the error estimation.

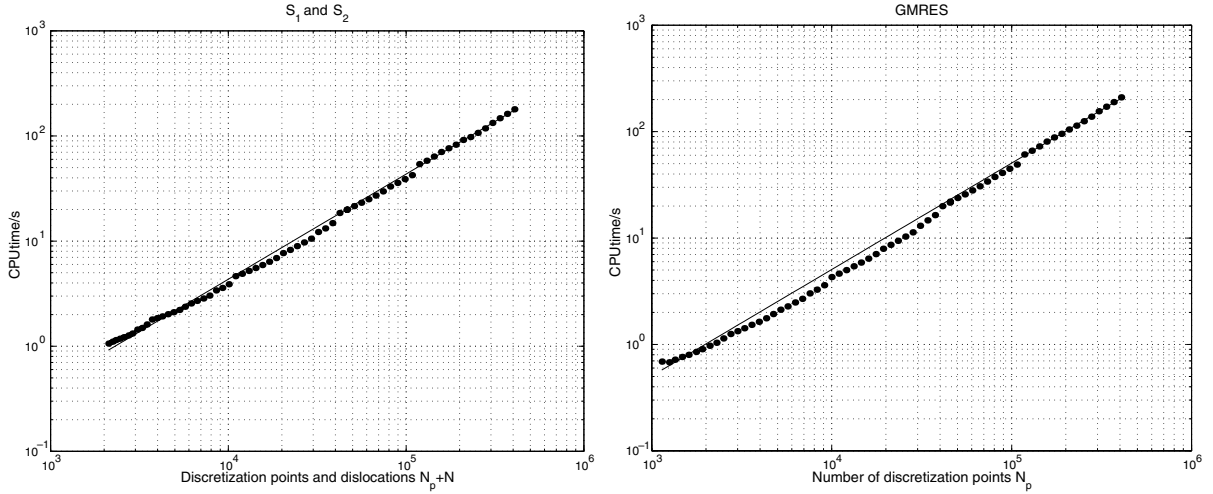


Fig. 5. CPU time in seconds required for the different parts of the simulation (\cdots) as a function of the number of components. Solid lines indicate linear proportionality. The number of dislocations is denoted as N and the number of discretization points as N_p . Left: time for computing S_1 and S_2 . Right: time per iteration for solving the discretized integral equation.

5.1. Uniaxial tensile loading

Uniaxial tensile loading simulations at three different loading rates are performed, at $\dot{\epsilon}_y^{\text{pr}}/E = 375, 500$ and 625 s^{-1} . The middle loading rate will be taken as reference, and denoted as 100% in the following. In all loading cases, a rectangular geometry, $2h = 12 \text{ }\mu\text{m}$ long and $2w = 4 \text{ }\mu\text{m}$ wide, is used. As a measure of the global strain, the difference between the average y -displacement along the short sides divided by the initial length of the specimen is used,

$$\hat{\epsilon}_{22} = \frac{1}{A} \left(\int_{-w}^w u_y(x, h) dx - \int_{-w}^w u_y(x, -h) dx \right). \quad (31)$$

A reference stress is introduced as

$$t_{\text{ref}} = f_{\text{mean}}/b, \quad (32)$$

and in this case, $t_{\text{ref}} = 50 \text{ MPa}$. The global strain $\hat{\epsilon}_{22}$ vs. normalized applied stress $t_y^{\text{pr}}/t_{\text{ref}}$ is presented in Fig. 6. The amount of plastic strain is computed as

$$\hat{\epsilon}^p = \hat{\epsilon}_{22} - t_y^{\text{pr}}(1 - \nu^2)/E.$$

Some observations from these simulations are worth mentioning. It can be noted that the yield

limit is independent of the loading rate. It is controlled by

$$\min_{k=1, \dots, N_s} f_k^{\text{nuc}}$$

since the stress state is homogeneous in the elastic regime. This means that the onset of plastic deformation will be a stochastic quantity in this model. A lower loading rate gives more yielding, and a higher loading rate gives less yielding at the same applied stress, see the left image of Fig. 6. This effect is limited by the low cut-off velocity v_{max} . The cut-off velocity is too low to give realistic predictions under the present loading conditions. The dislocation density $\rho = N/A$ is directly proportional to the amount of plastic strain, see the right image of Fig. 6. This has also been observed in experiments, see for example Ref. [36]. No clear effect of loading rate on the evolution of ρ as a function of $\hat{\epsilon}^p$ can be seen.

The number of dislocations present in the model when the simulations are terminated are 626, 1047 and 962 for the three loading rates studied. The number of discretization points on the boundary, N_p , in the simulations varied between 352 and 3192 due to the adaptive scheme. For dislocation positions at different strain levels, see Fig. 4.

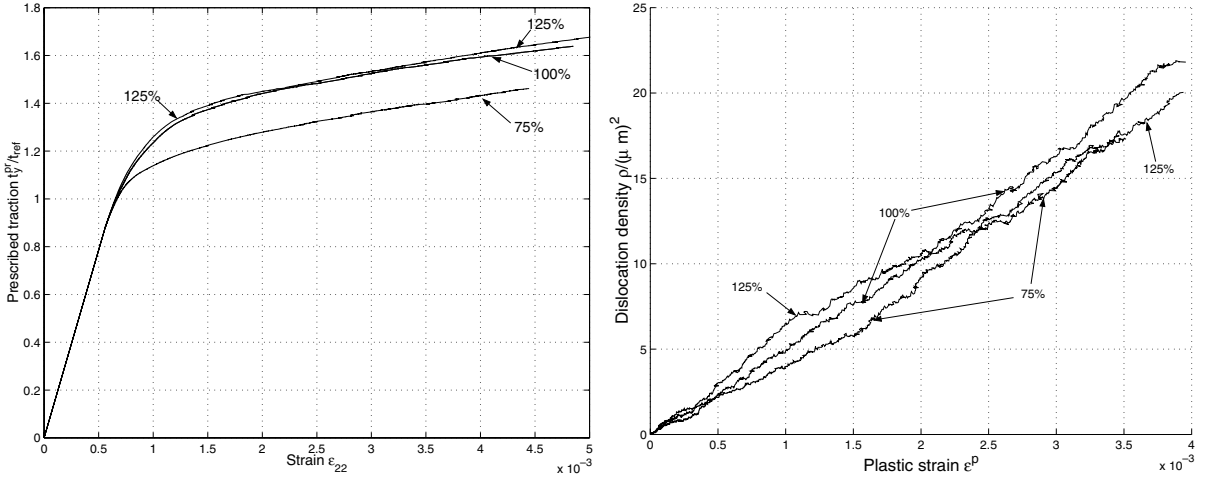


Fig. 6. Effect of loading rate. Left: Prescribed (normalized) traction versus strain for the uniaxial tension simulations. Right: Dislocation density versus plastic strain. 100% represent the reference loading rate, and 75% and 125% represent the lower and higher loading rates respectively.

5.2. Bending moment loading

Bending moment load simulations are performed at three loading rates, at $\dot{\sigma}_0/E = 375, 500$ and 625 s^{-1} , denoted as the 75%, 100% and 125% case. In all loading cases, a rectangular geometry, $2h = 12 \mu\text{m}$ long and $2w = 4 \mu\text{m}$ wide, is used. A linearly varying traction vector is applied, see Fig. 7,

$$t_y^{\text{pr}}(z, T) = \sigma_0(T) \frac{\Re\{z\}}{w} \text{sign}(\Im\{z\}), \quad (33)$$

giving a resulting moment per unit thickness,

$$M(T) = \frac{2}{3} \sigma_0(T) w^2. \quad (34)$$

This load corresponds to pure bending in the elastic case, that is when no dislocations are present. When dislocations are present, this load will cause a deformation reasonably similar to pure bending. A reference moment M_{ref} is introduced as

$$M_{\text{ref}} = \frac{2}{3} \frac{f_{\text{mean}}}{b} w^2. \quad (35)$$

As a measure of the rotation angle θ of the short side, a least square fit of a straight line to the

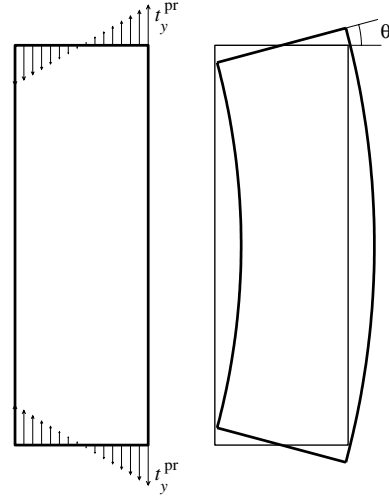


Fig. 7. Left: Prescribed traction for the bending moment load simulations. Right: Definition of the rotation angle θ . The thicker line indicates the deformed configuration.

displacement of the short sides is used. The rotation of the sides $y = \pm h$ is computed as

$$\theta(\pm h) = \arctan \frac{|\zeta(\pm h)|}{\eta(\pm h)}, \quad (36)$$

where the intermediate quantities ζ and η are introduced according to

$$\zeta(\pm h) = \int_{-w}^w (u_y(x, \pm h) - \tilde{u}_y(\pm h)) \times (\xi(x, \pm h) - \tilde{\xi}(\pm h)) dx \quad (37)$$

and

$$\eta(\pm h) = \int_{-w}^w (\xi(x, \pm h) - \tilde{\xi}(\pm h))^2 dx. \quad (38)$$

The quantity ξ is the x -position in the deformed configuration,

$$\xi(x, y) = x + u_x(x, y). \quad (39)$$

In Eqs. (37) and (38), \tilde{u}_y denotes the mean y -displacement, and $\tilde{\xi}$ is the mean value of ξ . The rotation is then the mean of the rotations of the short sides $y = \pm h$,

$$\theta = \frac{1}{2}(\theta(h) + \theta(-h)). \quad (40)$$

The rotation angle θ vs. applied normalized moment M/M_{ref} and the dislocation density $\rho = N/A$ vs. rotation angle θ is presented in Fig. 8. The obtained dislocation densities shows fair agreement with those in Ref. [11]. For $\theta = 0.0175$, the present author obtained $\rho = 14.4 \mu\text{m}^{-2}$ for the reference loading rate, while Ref. [11] reports $\rho = 15.6 \mu\text{m}^{-2}$ for the same rotation angle. Also the dislocation distributions, see Fig. 9, are in

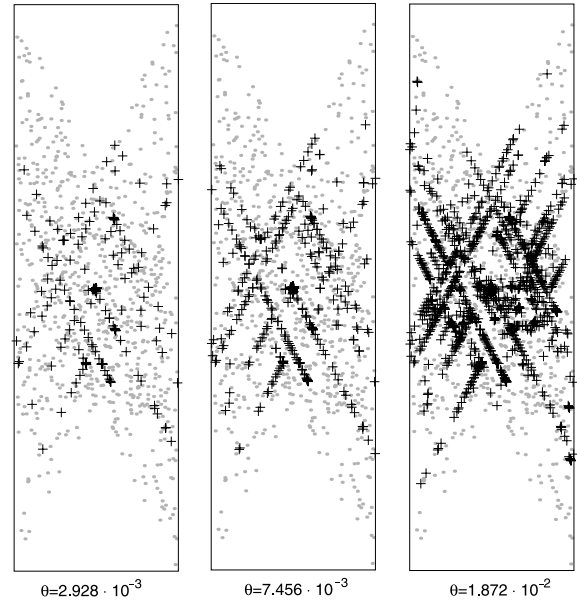


Fig. 9. Dislocation positions, indicated by '+', at different rotation angles. Dislocation sources are shown as grey dots.

principal agreement with Ref. [11]. The difference in boundary conditions between Ref. [11] and the present paper is probably the chief reason for the difference in the results. It can also be noted that the distribution is much more ordered in the bending moment case than in the uniaxial tension

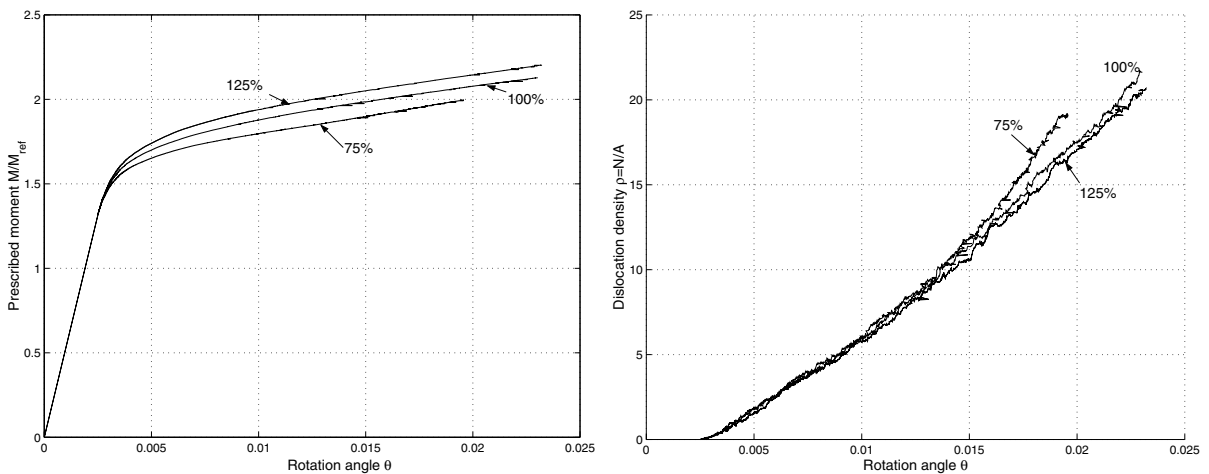


Fig. 8. Effect of loading rate. Left: Prescribed (normalized) moment versus rotation angle for the bending moment load simulations. Right: Dislocation density $\rho = N/A$ versus rotation angle θ .

case. Most of the dislocations are geometrically necessary.

The onset of plastic deformation is, just as for the uniaxial tension simulations, a stochastic quantity. The loading rate effect on the $\theta(M)$ behavior can be seen in the left image of Fig. 8. A higher loading rate gives less yielding, and a lower loading rate gives more yielding at the same applied moment. This effect is more pronounced in the bending moment case than in the uniaxial tension case, cf. Fig. 6. The effect of loading rate on the dislocation density is less pronounced. The 100% and the 125% case show very similar evolution of the dislocation density, while the 75% case shows a higher dislocation density.

The number of dislocations present in the model when the simulations are terminated are 938, 1039 and 988 for the three studied loading rates. The number of discretization points in the simulations varied between 944 and 5920 due to the adaptive scheme.

Remark 5.1. The prescribed traction boundary condition of Eq. (33) is chosen, since the Eq. (7) cannot handle mixed boundary conditions. Other types of boundary conditions will be studied in forthcoming work. Linearly varying displacement along the short sides was used in Ref. [11].

5.3. Effect of finite size

In order to study the effect of finite size, a bending moment load simulation of a specimen with height $2h = 24 \mu\text{m}$ and width $2w = 8 \mu\text{m}$ is performed, and the results are compared to those for a specimen with $2h = 12 \mu\text{m}$ and $2w = 4 \mu\text{m}$. The loading rate was $\dot{\sigma}_0/E = 500 \text{ s}^{-1}$, denoted as the 100% case in Section 5.2. The density of dislocation sources $\rho_s = N_s/A$ is the same for both specimen sizes. It is difficult to compare the results directly, due to the randomness in source placement and strength. Despite this, effects of finite size can be seen. The larger specimen shows a clearly softer behavior, with more yielding for the same applied moment, see the left image of Fig. 10. This is in agreement with well-known experimental results. However, it is not expected that a Hall–Petch relation for the yield limit should be reproduced. In the present model, the onset of plastic deformation is a stochastic quantity, controlled by the random placement and strength of dislocation sources.

In order to compare the dislocation densities, the plastic curvature κ^p is introduced

$$\kappa^p = \frac{\theta - M/D}{h}, \quad (41)$$

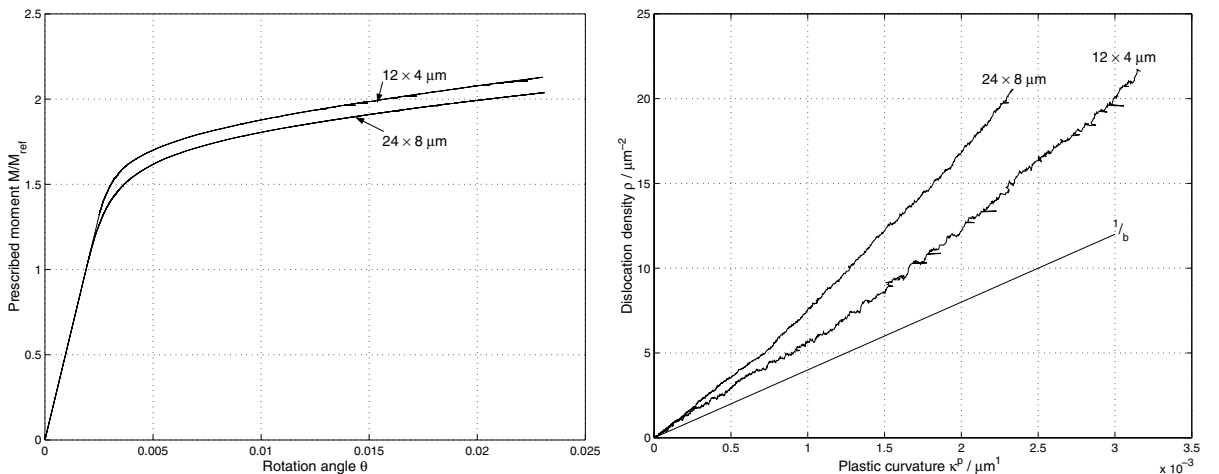


Fig. 10. Effect of finite size. Left: Prescribed normalized moment vs. rotation angle. Right: Dislocation density ρ as a function of the plastic curvature κ^p for the two different sizes studied. The slope $1/b$ is indicated by a dashed line.

where D is the elastic bending stiffness of the specimen. A comparison of the dislocation density ρ as a function of κ^p is shown in the right image of Fig. 10. The theoretical result for the density of geometrically necessary dislocations is $\rho_G = \kappa^p/b$ [37,38]. A least square fit to a linear relation for the smaller specimen results in $\rho = 1.6\kappa^p/b$. This means that about 63% of the dislocations are geometrically necessary. This is in fair agreement with Ref. [11], which reports that about 66% of the dislocations are geometrically necessary. For the larger specimen, a least square fit gives $\rho = 2\kappa^p/b$, which means that 50% of the dislocations are geometrically necessary.

The reason for the softer response of the larger specimen is probably that it contains more dislocation sources than the small one. A larger number of (mobile) dislocations is produced, which leads to more plastic deformation. Since dislocation sources are placed randomly with random nucleation strengths, it is difficult to draw conclusions from comparing only two simulations. A series of simulations must be studied in order to isolate stochastic effects. Results from this will be presented in future work.

For the bigger specimen, 4000 dislocations are present in the model when the simulation is terminated.

5.4. Error estimation

In order to estimate the pointwise error in the average strain $\hat{\epsilon}_{22}$ and the rotation angle θ obtained from the simulations, convergence studies are performed. A tolerance of 10^{-15} is used for the GMRES iterative solver and 10^{-16} for the FMM. The convergence studies are performed with uniform discretization, see the left image of Fig. 2. The a priori mesh refinement of Section 4.1 is not invoked. Convergence plots are shown in Fig. 11.

For the uniaxial strain simulation, one setup from the 100% case with $t_y^{\text{pr}}/t_{\text{ref}} = 1.65305644$ containing 979 dislocations is studied. This is a difficult setup, and it is assumed to give an estimate of the pointwise error for all steps of the simulation. The relative error in $\hat{\epsilon}_{22}$ is found to be 2.2×10^{-4} in the studied step. In the simulation 3184 points are used, resulting in $\hat{\epsilon}_{22} = 4.9195 \times 10^{-3}$. A fully converged result, $\hat{\epsilon}_{22} = 4.91842309492 \times 10^{-3}$, is obtained with 50 000 points or more. From this, it is estimated that the relative error is on the order of 5×10^{-4} in the uniaxial strain results of Fig. 6.

For the bending moment load simulation, one setup from the 125% case with $M/M_{\text{ref}} = 2.1516875$ containing 838 dislocations is studied. This is assumed to be a representative setup, giving

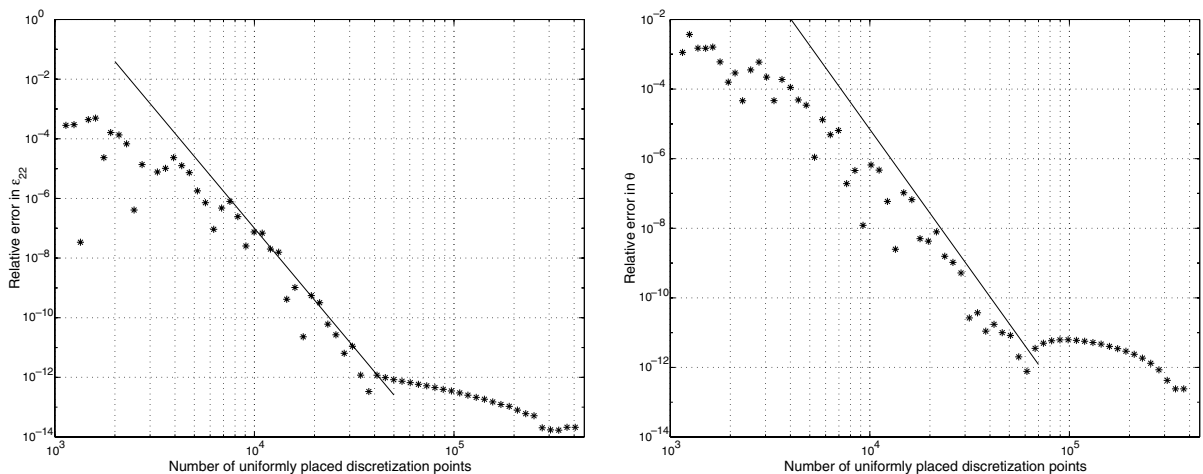


Fig. 11. Left: Convergence plot for the uniaxial strain simulation. The relative error in $\hat{\epsilon}_{22}$ of Eq. (31) vs. the number of uniformly placed discretization points. Right: Convergence plot for the bending moment load simulation. The relative error in θ of Eq. (40) vs. the number of uniformly placed discretization points. In both plots, a solid line indicates eight order convergence.

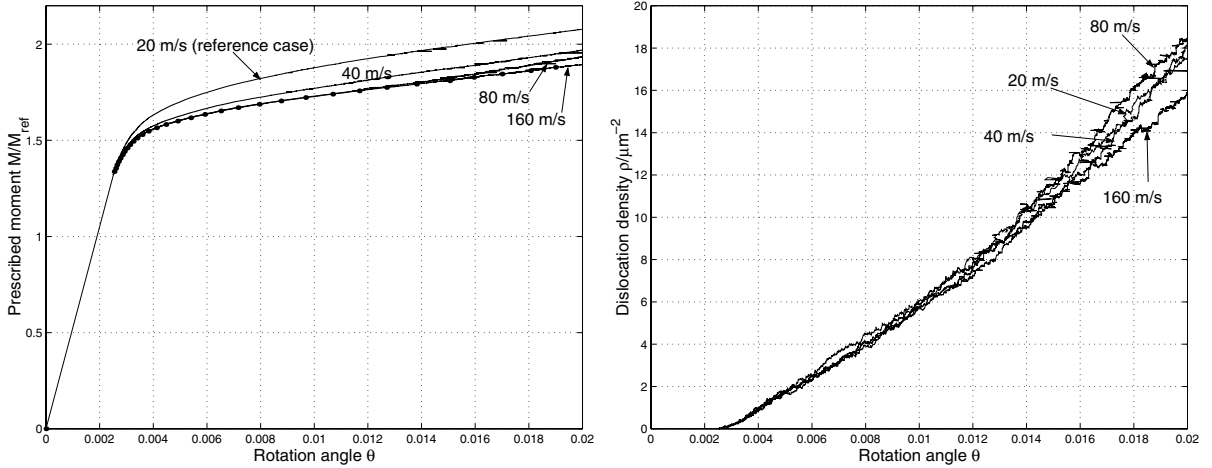


Fig. 12. Effect of v_{max} . Left: Prescribed normalized moment M/M_{ref} vs. rotation angle θ . An increase of v_{max} results in a softer response. The curve for $v_{\text{max}} = 160$ m/s is marked with dots. Right: Dislocation density ρ as a function of the rotation angle θ . The evolution of the dislocation density seems to be less affected by v_{max} .

an estimate of the pointwise error for all steps in the simulation. The relative error in θ in this step is found to be 8.8×10^{-6} . In the simulation, 4328 points are used, resulting in $\theta = 2.0362 \times 10^{-2}$. Totally 61 000 points or more are required for a fully converged result of $\theta = 2.03618572861 \times 10^{-2}$. The relative error in the bending results of Figs. 8, 10 and 12 is estimated to be on the order of 5×10^{-5} .

The order of convergence in the spatial discretization for the present algorithm is high, asymptotically eight in both the bending moment case and the uniaxial tension case, at least down to a relative error on the order of 10^{-12} . The operator H , cf. Eqs. (7) and (9), which is eight order accurate on smooth parts of the boundary, gives the major contribution to the error down to the order of 10^{-12} . After this, effects of the corner interaction becomes important, and the convergence stagnates.

It should be noted that very high accuracy is obtainable if enough discretization points are used, but there will always be a tradeoff between accuracy and execution time. The number of GMRES iterations are increased from about 22 to about 45 if the tolerance is reduced from 10^{-7} to 10^{-15} . More discretization points increases execution time, but increased tolerance in the FMM will also

require more time, since the FMM used in this algorithm is approximately $O((\ln \text{tol})^2)$ where the tolerance is denoted as tol .

In the convergence studies, up to 450 000 discretization points are used. This shows that the present algorithm can handle large scale computations.

Remark 5.2. The accuracies presented in this section might seem surprisingly high, but they are not unrealistic. Extremely accurate solutions to similar problems have previously been obtained using numerical methods based on the discretization of Fredholm second-kind integral equations, see Refs. [23,30,34,39]. Such numerical methods are very stable. The stability follows from the error estimate of Eq. (29), which means that the discretization error will decrease rapidly as N_p is increased, and that the condition number of $(\mathbf{I} - \mathbf{M})$ is bounded independent of N_p [31,32], which means that round-off errors will not increase as N_p is increased.

5.5. Effect of L_s

A few simulations are performed in order to study the effect of v_{max} and $L_s = v_{\text{max}} \Delta T$ on the simulation results.

Table 1
The effect of ΔT on the results from the bending moment load simulation

$\Delta T/5 \times 10^{-10}$	L_s/L_e	M/M_{ref}	θ	$\rho/\mu\text{m}^{-2}$
1.0	5	1.4005	2.697×10^{-3}	0.1042
0.5	2.5	1.4005	2.697×10^{-3}	0.1042
0.25	1.25	1.4005	2.697×10^{-3}	0.1042
1.0	5	1.7001	5.001×10^{-3}	1.750
0.5	2.5	1.7001	5.012×10^{-3}	1.875
0.25	1.25	1.7001	5.014×10^{-3}	1.417
1.0	5	2.00005	1.573×10^{-2}	12.06
0.5	2.5	2.00005	1.629×10^{-2}	12.53
0.25	1.25	2.00005	1.664×10^{-2}	11.94

Two additional bending moment simulations with $\Delta T = 1.25 \times 10^{-10}$ and 2.5×10^{-10} s were performed in order to investigate the effect of ΔT on the global error in the bending moment simulations. Results from these simulations are compared to the reference case with $\Delta T = 5 \times 10^{-10}$ s in Table 1. For the three simulations compared, all other parameter values were identical, that is $v_{\text{max}} = 20$ m/s, $2h = 12$ μm and $2w = 4$ μm . The loading rate was $\dot{\sigma}_0/E = 500$ s $^{-1}$. These parameter values results in $L_s = 1.25L_e, 2.5L_e$ and $5L_e$ respectively. It is concluded that for the three cases compared, the effect of ΔT is not significant. The qualitative predictions are identical, and only minor quantitative differences are obtained. The moment vs. rotation curves for the three cases are almost coincident. The biggest differences are obtained in the dislocation density vs. rotation curves, where the simulation using $\Delta T = 1.25 \times 10^{-10}$ s time step predicts 10% lower dislocation density than the simulation using $\Delta T = 5 \times 10^{-10}$ s for the same rotation angle. It can be noted that the differences in dislocation density vs. moment are much smaller, see Table 1.

In the reference case, the cut-off velocity $v_{\text{max}} = 20$ m/s is chosen. The maximum dislocation velocity is physically limited by the shear wave velocity in the material, typically on the order of 10^3 m/s. The maximum distance one dislocation can move in one time step $L_s = v_{\text{max}}\Delta T$ must not be too long, or dislocation interactions might be missed. The low value $v_{\text{max}} = 20$ m/s makes it possible to take longer (and thus fewer) time steps,

reducing the simulation execution time. Three bending moment simulations with $v_{\text{max}} = 40, 80$ and 160 m/s were performed in order to investigate the effect of the cut-off velocity on the bending moment simulation results. In these simulations, $L_s = 5L_e$ was used. All other parameter values were identical to the reference case. As can be seen from the left image of Fig. 12, an increase of v_{max} results in a softer response, that is more deformation at the same load, at least up to a limit. The curves for $v_{\text{max}} = 80$ and 160 m/s are nearly coincident, at least for $\theta \leq 0.015$. From this it is concluded that if $v_{\text{max}} \geq 80$ m/s the simulation results are (nearly) independent of v_{max} for the present loading rate. The dislocation density vs. rotation curve is less affected by the cut-off velocity, see the right image of Fig. 12. There is no clear trend in the influence of the cut-off velocity on the dislocation density evolution. The curves for 20 and 40 m/s are nearly coincident in the studied interval, and the 80 m/s curve does not differ significantly from the two first curves. Increasing v_{max} to 160 m/s results in a clearly lower ρ for $\theta > 0.015$. This can be explained by that more dislocations leave the specimen due to the higher cut-off velocity.

Using a too low cut-off velocity can overestimate the hardening behavior of the specimen. The effect of the time step length is less prominent. The cut-off velocity v_{max} as it appears in Eq. (21) is a physically motivated model parameter, while the time step ΔT is more artificial. From this, it is natural that v_{max} has a bigger influence on the results than ΔT .

6. Conclusions

An efficient numerical algorithm for dislocation dynamics simulations in 2D is presented. Linear complexity is obtained by use of the fast multipole method throughout the algorithm. Agreement with previous results in the literature is established. The dislocation dynamics model can capture both loading rate and size effects on the plastic response, and the simulation results are in agreement with what is well known from experiments. The presented algorithm can be used as tool for understanding the fundamentals of dislocation behavior, and also for developing non-local plasticity models.

Convergence studies show the numerical stability of the algorithm, and that high accuracy is obtainable. Error estimates are given. The order of convergence for the present algorithm is high, and it can handle large scale computations.

The parameter studies of Section 5 shows that a rather high cut-off velocity, $v_{\max} \geq 80$ m/s, is required to obtain bending moment load simulation results independent of v_{\max} . Using a too low cut-off velocity will overestimate the hardening behavior of the specimen studied. The use of an efficient numerical method makes an eightfold increase of v_{\max} possible. Previous results were obtained using $v_{\max} = 20$ m/s, which then was estimated to be sufficient. The other parameters studied, ΔT and L_s , have a less prominent effect on the simulation results.

An $O(N)$ algorithm for dislocation dynamics in 2D has previously been presented by Wang and LeSar, see Ref. [16]. They studied periodic boundary conditions, and were in general more focused on the implementation of the multipole method. It should be mentioned that the effect of specimen size cannot be studied using periodic boundary conditions, but are applicable if the bulk mechanical behavior is of interest. Rodin [40] showed that the FMM can be applied to compute the elastic interactions between dislocations in 3D. However, no boundary value problem was solved. To the knowledge of the present author, the FMM has not previously been used for dislocation simulations in a finite domain.

Even though the present algorithm has many good properties, there are some improvements that

should be considered. The presented simulations are performed using a SUN Enterprise workstation and sequential computing. The use of parallel computing could probably increase speed even more. Since a standard multipole method is used, time could also be saved by customizing and optimizing the multipole method for the present purposes.

Also, extensions of the dislocation dynamics model itself should be considered. This could be to include obstacles to dislocation movement, some evolution of the source density ρ_s , and dislocation climb, that is the possibility of dislocation motion perpendicular to the slip planes. It would also be of interest to study dislocation behavior in polycrystals, and the effect of grain boundaries on dislocation movement. As mentioned above, a cut-off velocity of at least 80 m/s is recommended. A possible way of reducing simulation execution time could be to introduce adaptivity in the time step length in some way. Another possible extension is the consideration of other boundary conditions, for example prescribed displacement. The modeling of grain boundaries and the extension of the model to 3D are other interesting options. Dislocation dynamics simulations in 3D has been presented by for example Devincre and Kubin [41]. Discrete dislocation models have also been used for studying fatigue crack growth, see for example Refs. [10,42,43].

Acknowledgements

The financial support from TFR, NFR and the Knut and Alice Wallenberg foundation under contract 98-568 is gratefully acknowledged. The author would also like to thank Dr. Adam Wikström, Dr. Harko Cleveringa and Prof. Peter Gudmundson for stimulating discussion about dislocations, simulations and plasticity in general.

References

- [1] N.A. Fleck, G.M. Muller, M.F. Ashby, J.W. Hutchinson, Strain gradient plasticity: theory and experiments, *Acta Metallurgica et Materialia* 42 (1994) 475–487.

- [2] J.S. Stölken, A.G. Evans, A microbend test method for measuring the plasticity length scale, *Acta Materialia* 46 (1998) 5109–5115.
- [3] E.C. Aifantis, On the microstructural origin of certain inelastic models, *Journal of Engineering Materials Technology* 106 (1984) 326–330.
- [4] N.A. Fleck, J.W. Hutchinson, Strain gradient plasticity, *Advances in Applied Mechanics* 33 (1997) 295–360.
- [5] N.A. Fleck, J.W. Hutchinson, A reformulation of strain gradient plasticity, *Journal of the Mechanics and Physics of Solids* 33 (2001) 2245–2271.
- [6] A. Acharya, A model of crystal plasticity based on the theory of continuously distributed dislocations, *Journal of the Mechanics and Physics of Solids* 49 (2001) 761–784.
- [7] A. Menzel, P. Steinman, On the continuum formulation of higher gradient plasticity for single and polycrystals, *Journal of the Mechanics and Physics of Solids* 48 (2000) 1777–1796.
- [8] J.W. Hutchinson, Plasticity at the micron scale, *International Journal of Solids and Structures* 37 (2000) 225–238.
- [9] A. Needleman, Computational mechanics at the mesoscale, *Acta Materialia* 48 (2000) 105–124.
- [10] H.H.M. Cleveringa, E. Van der Giessen, A. Needleman, A discrete dislocation analysis of mode I crack growth, *Journal of the Mechanics and Physics of Solids* 48 (2000) 1133–1157.
- [11] H.H.M. Cleveringa, E. Van der Giessen, A. Needleman, A discrete dislocation analysis of bending, *International Journal of Plasticity* 15 (1999) 837–868.
- [12] H.H.M. Cleveringa, E. Van der Giessen, A. Needleman, Comparison of discrete dislocation and continuum plasticity predictions for a composite material, *Acta Materialia* 45 (1997) 3163–3179.
- [13] E. Van der Giessen, A. Needleman, Discrete dislocation plasticity: a simple planar model, *Modelling and Simulation in Materials Science and Engineering* 3 (1995) 689–735.
- [14] L. Greengard, V. Rokhlin, A fast algorithm for particle simulations, *Journal of Computational Physics* 73 (1987) 415–424.
- [15] J. Carrier, L. Greengard, V. Rokhlin, A fast and adaptive multipole algorithm for particle simulations, *SIAM Journal on Scientific and Statistical Computing* 9 (1988) 669–686.
- [16] H.Y. Wang, R. LeSar, $O(N)$ algorithm for dislocation dynamics, *Philosophical Magazine A* 71 (1995) 149–164.
- [17] S.G. Mikhlin, *Integral Equations*, Pergamon Press, London, 1957.
- [18] N.I. Muskhelishvili, *Some Basic Problems of the Mathematical Theory of Elasticity*, P. Noordhoff Ltd., Groningen 1953, London 1957.
- [19] V.Z. Parton, P.I. Perlin, *Integral Equation Methods in Elasticity*, MIR, Moscow, 1982.
- [20] I.S. Sokolnikoff, *Mathematical Theory of Elasticity*, McGraw-Hill, New York, 1956.
- [21] J. Weertman, J.R. Weertman, *Elementary Dislocation Theory*, The Macmillan Company, New York, 1965.
- [22] J. Helsing, On the interior stress problem for elastic bodies, *Journal of Applied Mechanics* 67 (2000) 658–664.
- [23] J. Helsing, A. Jonsson, On the computation of stress fields on polygonal domains with V-notches, *International Journal for Numerical Methods in Engineering* 53 (2002) 433–453.
- [24] A.N. Gulluoglu, D.J. Srolovitz, R. LeSar, P.S. Lomdal, Dislocation distributions in two dimensions, *Scripta Metallurgica* 23 (1989) 1347–1352.
- [25] J. Lepinoux, L.P. Kubin, Dynamic organization of dislocation structures: A simulation, *Scripta Metallurgica* 21 (1987) 833–838.
- [26] A.N. Gulluoglu, C.S. Hartley, Simulations of dislocation microstructures in two dimensions. I. Relaxed structures, *Modelling and Simulation in Materials Science and Engineering* 1 (1993) 1–17.
- [27] A.N. Gulluoglu, C.S. Hartley, Simulations of dislocation microstructures in two dimensions. II. Dynamic and relaxed structures, *Modelling and Simulation in Materials Science and Engineering* 1 (1993) 383–402.
- [28] J.Y. Shu, N.A. Fleck, E. VanderGiessen, A. Needleman, Boundary layers in constrained plastic flow: comparison of nonlocal and discrete dislocation plasticity, *Journal of the Mechanics and Physics of Solids* 49 (2001) 1361–1395.
- [29] J. Helsing, Thin bridges in isotropic electrostatics, *Journal of Computational Physics* 127 (1996) 142–151.
- [30] L. Greengard, J. Helsing, On the numerical evaluation of elastostatic fields in locally isotropic two-dimensional composites, *Journal of the Mechanics and Physics of Solids* 46 (1998) 1441–1462.
- [31] K.E. Atkinson, *The Numerical Solution of Integral Equations of The Second Kind*, Cambridge University Press, Cambridge, 1997.
- [32] W. Hackbush, *Integral Equations*, Birkhäuser, Basel, 1995.
- [33] M.L. Williams, Stress singularities resulting from various boundary conditions in angular corners of plates in extension, *ASME Journal of Applied Mechanics* 19 (1952) 526–528.
- [34] J. Helsing, A. Jonsson, A seventh order accurate and stable algorithm for the computation of stress inside cracked rectangular domains, Report 304, Department of Solid Mechanics, KTH 2002.
- [35] Y. Saad, M.H. Schultz, GMRES: a generalized minimum residual algorithm for solving nonsymmetric linear systems, *SIAM Journal of Scientific and Statistical Computing* 7 (1986) 856–869.
- [36] M. Hommel, O. Kraft, Deformation behavior of thin copper films on deformable substrates, *Acta Materialia* 49 (2001) 3935–3947.
- [37] J.F. Nye, Some geometrical relations in dislocated crystals, *Acta Metallurgica* 1 (1953) 153–162.
- [38] M.F. Ashby, The deformation of plastically non-homogeneous materials, three-dimensional dislocations, *Philosophical Magazine* 21 (1970) 399–424.
- [39] J. Helsing, A. Jonsson, Stress computations on multiply connected domains, *Journal of Computational Physics* 176 (2002) 456–482.

- [40] G.J. Rodin, Towards rapid evaluation of the elastic interactions among three-dimensional dislocations, *Philosophical Magazine Letters* 77 (1998) 187–190.
- [41] B. Devincre, L.P. Kubin, Mesoscopic simulation of dislocations and plasticity, *Materials Science and Engineering A* 234–236 (1997) 8–14.
- [42] F.O. Reimelmoser, P. Gumbsch, R. Pippan, Plastic deformation at short edge cracks under fatigue loading, *Engineering Fracture Mechanics* 66 (2000) 357–374.
- [43] V.S. Deshpande, E. Van der Giessen, A. Needleman, A discrete dislocation simulation of near-threshold fatigue crack growth, *Acta Materialia* 49 (2001) 3189–3203.